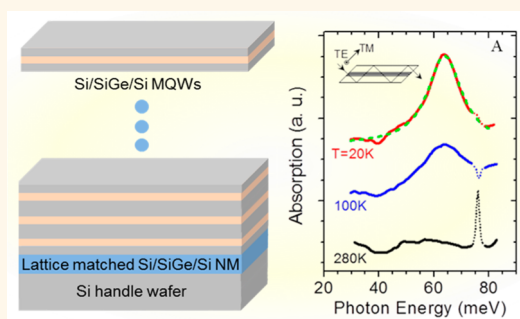


Strain Engineered SiGe Multiple-Quantum-Well Nanomembranes for Far-Infrared Intersubband Device Applications

Pornsatit Sookchoo,[†] Faisal F. Sudradjat,[‡] Arnold M. Kiefer,[†] Habibe Durmaz,[‡] Roberto Paiella,^{‡,*} and Max G. Lagally^{†,*}

[†]University of Wisconsin-Madison, Madison Wisconsin 53706, United States and [‡]Boston University, Boston, Massachusetts 02215, United States

ABSTRACT SiGe/Si quantum wells are of great interest for the development of Group-IV THz quantum cascade lasers. The main advantage of Group-IV over III–V materials such as GaAs is that, in the former, polar phonon scattering, which significantly diminishes the efficiency of intersubband light emission, is absent. However, for SiGe/Si multiple-quantum-well structures grown on bulk Si, the lattice mismatch between Si and Ge limits the critical thickness for dislocation formation and thus the number of periods that can be grown. Similarly, the use of composition-graded SiGe films as a lattice-matched substrate leads to the transfer of dislocations from the graded buffer substrate into the quantum wells, with a consequent decrease in light emission efficiency. Here we instead employ nanomembrane strain engineering to fabricate dislocation-free strain relaxed substrates, with lattice constants that match the average lattice constants of the quantum wells. This procedure allows for the growth of many periods with excellent structural properties. The samples in this work were grown by low-pressure chemical vapor deposition and characterized *via* high-resolution X-ray diffraction and far-infrared transmission spectroscopy, showing narrow intersubband absorption features indicative of high crystalline quality.



KEYWORDS: semiconductor nanomembranes · SiGe/Si quantum wells · intersubband transitions · strain engineering · epitaxy

SiGe quantum wells (QWs) are promising candidates for the development of far-infrared intersubband (ISB) optoelectronic devices, including quantum cascade (QC) lasers.¹ Intersubband transitions in QWs involve low-dimensional electronic states derived from the same energy band (typically the conduction band), and as a result the nature of the bandgap of the QW materials is irrelevant to their radiative efficiency. Therefore, the QC-laser scheme provides a promising approach for the demonstration of laser action in indirect-bandgap semiconductors such as Si, Ge, and SiGe, where light emission *via* interband transitions is exceedingly inefficient. In fact, group-IV semiconductors are particularly attractive for the development of QC lasers operating at THz wavelengths, by virtue of their nonpolar nature. Specifically, thermally activated electron/LO-phonon polar interactions, which limit the operation of

existing GaAs/AlGaAs THz QC lasers to cryogenic temperatures,^{2,3} are absent in nonpolar materials. In addition, the lack of photon/optical-phonon interactions in these materials allows for operation across the entire THz spectrum, whereas III–V semiconductors are fundamentally precluded from emission within their Reststrahlen band (typically in the THz range). Therefore, Si-based THz QC lasers can in principle provide higher operating temperatures and broader wavelength coverage than existing III–V devices, as needed to overcome the present lack of practical THz sources for applications in security screening, biochemical sensing, medical diagnostics, and manufacturing quality control.⁴ Furthermore, by virtue of their intrinsic CMOS compatibility, group-IV ISB devices could be readily integrated in complex Si-based microelectronic systems to provide unprecedented functionality and miniaturization.

* Address correspondence to
rpaiella@bu.edu,
lagally@engr.wisc.edu.

Received for review November 29, 2012
and accepted February 12, 2013.

Published online February 12, 2013
10.1021/nn305528t

© 2013 American Chemical Society

Motivated by these considerations, extensive research efforts have been devoted to SiGe QC structures in the past several years, leading to the demonstration of ISB electroluminescence at mid-infrared^{5–7} and THz⁸ wavelengths. Most of these activities have focused on hole ISB transitions in SiGe/Si QWs, as in these heterostructures the valence band offsets are generally larger than the conduction band discontinuities, and therefore holes can experience stronger quantum confinement than electrons.^{9,10} More recently, electronic ISB transitions in the *L* valleys of Ge/SiGe QWs have also started to gain attention,^{11–13} owing to potential advantages of longer nonradiative decay lifetimes and larger oscillator strengths. In any case, ISB population inversion and laser action in SiGe QC structures have not yet been demonstrated, mostly because of structural-quality issues related to the large (4.2%) lattice mismatch between Si and Ge. In devices requiring a large number of QWs, such as QC lasers, the resulting accumulated strain generally relaxes through the formation of misfit dislocations and other structural defects, which strongly degrade electrical and optical properties.

To attempt to address this issue, more recent experimental realizations of SiGe/Si QC light emitters⁷ have been grown on composition-graded SiGe buffer layers plastically relaxed on Si. This approach allows growing thicker multiple-QW active layers, with small (ideally zero) net strain per period if the final composition of the graded buffer matches the average composition of the QC material. The structural quality of the resulting strain compensated samples, however, was still inadequate for QC laser development,¹ as evidenced, for example, by their relatively large ISB emission linewidths. This result can be largely ascribed to the non-negligible density of misfit dislocations that are necessarily created in the SiGe substrates during their growth and strain relaxation.¹⁴ Such dislocations produce lateral strain inhomogeneities caused by dislocation pileup and a mosaic structure, as well as a rough surface morphology (cross-hatch) that requires chemical-mechanical polishing. More importantly, strain inhomogeneities and dislocation threads propagate into the overlaying epitaxial layers, ultimately limiting device performance.

In this article, we report a novel approach for the development of high-quality SiGe multiple-QW structures, where the QWs are grown on a strain relaxed SiGe multilayer nanomembrane (NM) that is at some stage during its fabrication free-standing, so that strain can be shared elastically among its individual layers.¹⁵ The procedure for fabrication of such NM substrates is based on a technology that has been developed in recent years for a wide range of fundamental materials studies and device applications.¹⁶ With this technology, single-crystal semiconductor sheets with nanoscale thicknesses are released from their original

substrates *via* the selective etch of an underlying sacrificial layer, leading to the formation of free-standing NMs of exceptional robustness and flexibility. If the NM contains different layers of lattice-mismatched materials under strain (Si and Si_{0.79}Ge_{0.21} in our case), strain relaxation can occur upon NM release *via* strain sharing among the constituent layers, rather than through the formation of defects.¹⁵ Correspondingly, the NM in-plane lattice constant relaxes to the value that minimizes the overall strain in the constituent layers. In a recent report, a similar procedure has been used for the development of “bulk” SiGe NMs, in effect creating a defect-free crystal of the latter alloy material.¹⁷

On the basis of this general idea, multilayer SiGe/Si NMs with the desired lattice constant can be formed, to be used as a template for the subsequent strain compensated growth of arbitrarily thick multiple-QW structures. At the same time, unlike the aforementioned composition graded SiGe buffer layers, these NMs are free of threading dislocations that would otherwise propagate into the QWs. In the present work, we have used this approach to grow a 45-period Si_{0.79}Ge_{0.21}/Si multiple-QW structure designed to provide hole ISB absorption at a photon energy of about 58 meV (*i.e.*, 21- μ m wavelength, 14-THz frequency). X-ray diffraction (XRD) data demonstrate elastic relaxation *via* strain sharing in the NM, and indicate good structural quality of the QWs grown on this substrate. Furthermore, far-infrared transmission spectroscopy measurements reveal a pronounced absorption peak near the target ISB transition wavelength, with substantially narrower line width compared to the ISB absorption spectrum of a similar QW structure grown under the same conditions on a bulk Si substrate. These results therefore confirm the suitability of the proposed fabrication approach for the development of far-infrared ISB devices based on SiGe QWs.

RESULTS AND DISCUSSION

The specific multiple-QW structure developed in this work consists of 45 repetitions of 7.0-nm-thick Si_{0.79}Ge_{0.21} wells separated by 33.0-nm-thick Si barriers grown along the (001) crystallographic direction. A portion of each barrier is doped p-type with boron to the level of 7×10^{17} cm⁻³, so that a sufficiently large density of holes can be established in the ground-state subband of each QW for strong ISB absorption. A schematic cross-sectional view of one QW repeat unit is shown in Figure 1A. The resulting valence band diagram is plotted in Figure 1B, as computed with a self-consistent Schrödinger-Poisson equation solver based on a 6×6 Luttinger-Kohn model.¹⁸ In this plot, the solid and dashed black lines correspond to the heavy-hole (HH) and light-hole (LH) valence band edges, respectively. The strong bending observed in these band lineups is a direct consequence of the

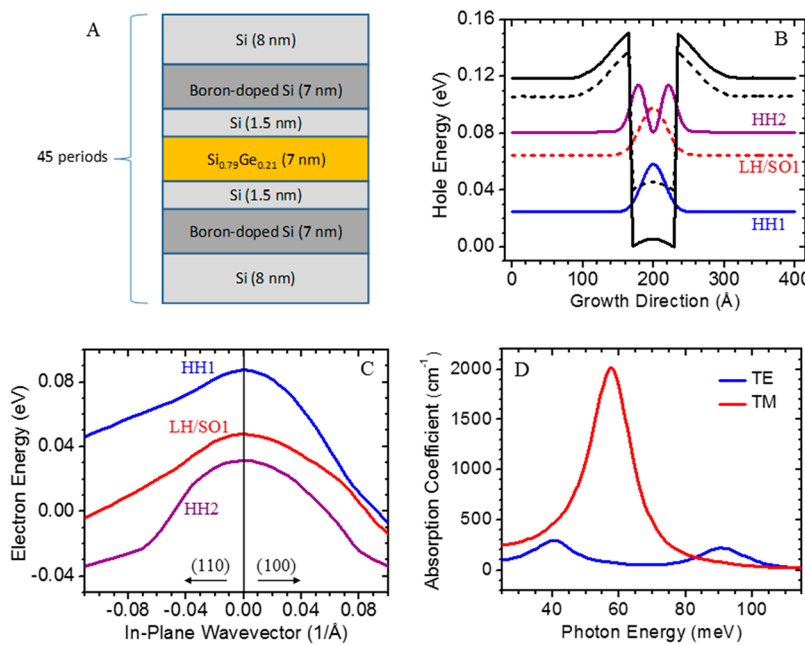


Figure 1. Layer sequence, valence subband structure, and calculated absorption spectrum of the SiGe/Si multiple-QW sample developed in this work. (A) Schematic cross-sectional view of one QW period. (B) Calculated valence-band lineup and squared envelope functions of the lowest-energy hole subbands. The vertical axis in this figure corresponds to hole (rather than electron) energy. (C) Electron-energy dispersion curves of the valence subbands of panel B. (D) Calculated low-temperature intersubband absorption spectrum of the same structure for transverse-electric (TE)- and transverse-magnetic (TM)-polarized light.

spatial separation between the ionized acceptor impurities and the holes (modulation doping), which is favorable for the purpose of reducing impurity scattering. The squared envelope functions of the lowest HH and mixed LH/spin-orbit-split-off (SO) valence subbands are also shown in Figure 1B, referenced to their respective energy levels. The corresponding energy dispersion curves along the (100) and (110) directions on the plane of the QWs are plotted in Figure 1C. It should be noted that the vertical axis in Figure 1B refers to hole energy, whereas the dispersion curves of Figure 1C correspond to electron energy plotted as a function of in-plane wavevector \mathbf{k}_t .

The energy eigenvalues and eigenfunctions shown in these figures can be used to calculate the QW ISB absorption coefficient using well-established formulas.¹⁹ The resulting low-temperature (10 K) absorption spectra are plotted in Figure 1D, where the blue and red lines correspond to transverse-electric (TE)- and transverse-magnetic (TM)-polarized light, that is, with electric field parallel and perpendicular to the growth direction, respectively. In computing these traces, a homogeneously broadened line width of 15 meV [full width at half-maximum (fwhm)] was assumed, as obtained from the experimental results described in the following. Furthermore, the photon energies of peak absorption were evaluated including many-body effects (specifically the depolarization and exciton shifts),¹⁹ which can produce a non-negligible correction in the type of samples considered in this work. The theoretical results shown in Figure 1D indicate that ISB

absorption in these QWs is dominated by transitions between the lowest two HH subbands (labeled HH1 and HH2 in Figure 1 panels B and C), at a photon energy of 58 meV. Consistent with well-known polarization selection rules,¹⁹ these HH ISB transitions can only couple to TM-polarized light. In contrast, the TE-polarized ISB absorption spectrum of Figure 1D has two peaks, centered at 41 and 91 meV, respectively. The former feature originates from transitions between subbands of the same parity (HH1 and LH/SO1), which are strictly forbidden for $\mathbf{k}_t = 0$, where the hole occupation probability of the initially occupied subband (HH1) is largest. The latter feature involves transitions into a LH/SO subband near the top of the barriers [not included in Figures 1B,C], whose envelope function is only weakly confined in the QW. As a result, both TE-polarized absorption peaks are relatively weak, and substantial ISB absorption in these QWs is only expected for TM-polarized light near 58 meV.

The sample fabrication process is illustrated schematically in Figure 2. The starting growth substrate is a commercially available (001) Si-on-insulator (SOI) wafer, with a 25-nm-thick top Si (template) layer that is thinned down to a thickness of 17 nm (Figure 2B). A thin epitaxial layer consisting of only five QW periods (*i.e.*, well below the critical thickness for plastic relaxation) is initially grown on this substrate, using low-pressure chemical vapor deposition (LPCVD) with silane, germane, and diborane precursors (Figure 2C). Because of its small thickness (and correspondingly small amount of accumulated strain), this heteroepitaxial

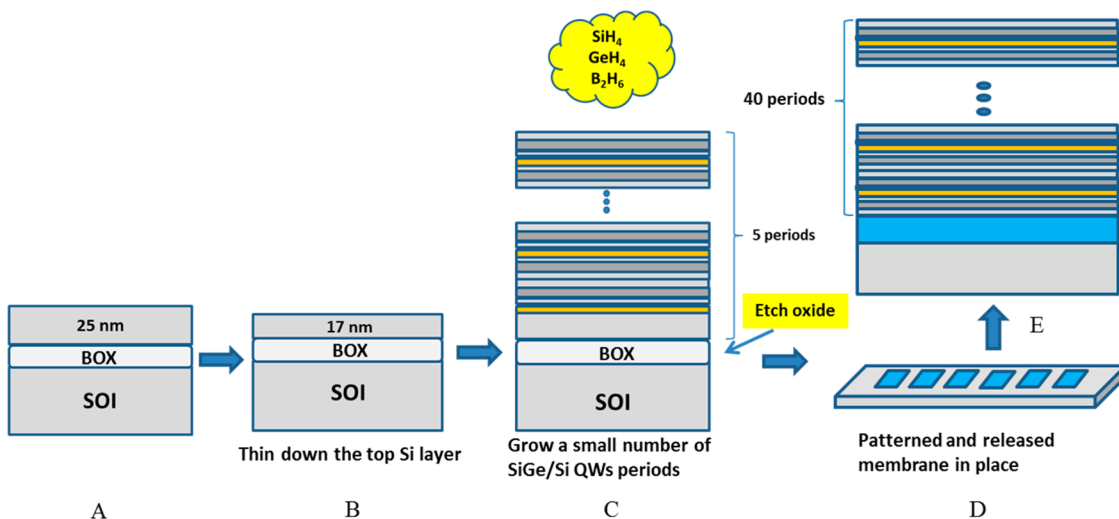


Figure 2. Schematic process for the development of strain compensated QWs on lattice matched NMs. The top Si layer of a SOI (001) substrate (A) is thinned to the desired thickness (B). The diagrams are not drawn to scale: the bottom handle wafer is much thicker than the Si top template layer. Five periods of the target SiGe/Si QW structure are grown by LPCVD on the same Si template layer, which is also used as the first barrier of the multiple-QW structure (C). The as-grown film is then patterned by lithography and the SOI buried oxide (BOX) is subsequently etched away with HF. As a result, rectangular-shaped Si/SiGe/Si/SiGe... NMs are released in place and in the process strain relaxation occurs *via* strain sharing among the constituent well and barrier layers (D). Finally, the NMs are bonded to the handle Si substrate by annealing at 450 °C for 1 h and used for the strain compensated growth of 40 more QW periods (E).

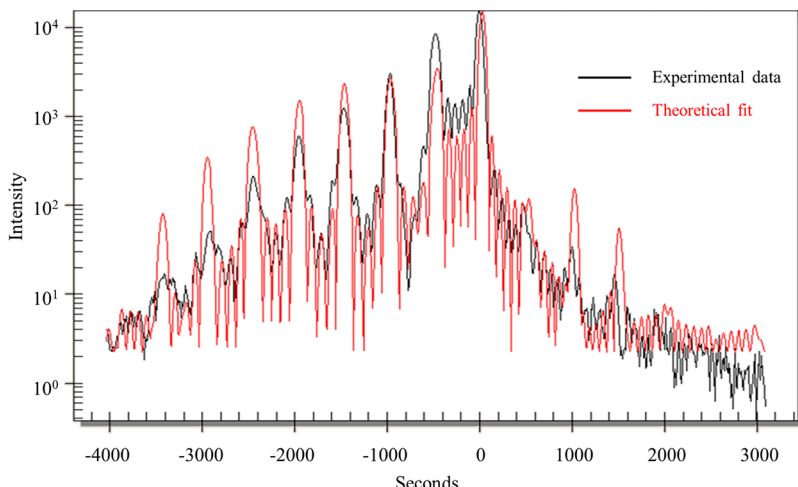


Figure 3. XRD scan from a 5-period SiGe/Si QW structure, and theoretical fit of the experimental data. The structure was grown on a SOI substrate but not released, so that no strain sharing has taken place. The fit is used to determine the layer thicknesses, compositions, and average strain.

film is fully pseudomorphic with respect to the SOI Si template layer, with no inelastic strain relaxation taking place through the formation of misfit dislocations. This expectation is confirmed *via* X-ray diffraction (XRD) analysis, as illustrated by the omega-2theta pattern shown in Figure 3. Several pronounced superlattice peaks, separated by subsidiary maxima, are clearly seen in this plot, indicating excellent crystalline quality. The layer thicknesses and compositions can also be accurately determined from these data.

At the same time, however, the number of QWs in these samples is far too small for practical ISB device applications. To enable the strain compensated growth of much thicker multiple-QW structures,

rectangular-shaped NMs consisting of the 5-period epitaxial film just described are then completely released from the SOI handle wafer, to be used as growth templates in a subsequent LPCVD run. To that purpose, the SOI buried oxide (BOX) layer is dissolved *via* wet etching in a hydrofluoric acid (HF) solution, after the NM boundaries and a pattern of small holes are lithographically defined through the semiconductor material to facilitate etchant access to the BOX. As the NMs are released from the SOI substrate, their internal stress due to the lattice mismatch between Si and $\text{Si}_{0.79}\text{Ge}_{0.21}$ is elastically relaxed *via* strain sharing. Specifically, the compressive strain in the $\text{Si}_{0.79}\text{Ge}_{0.21}$ well layers is partially relaxed through the introduction

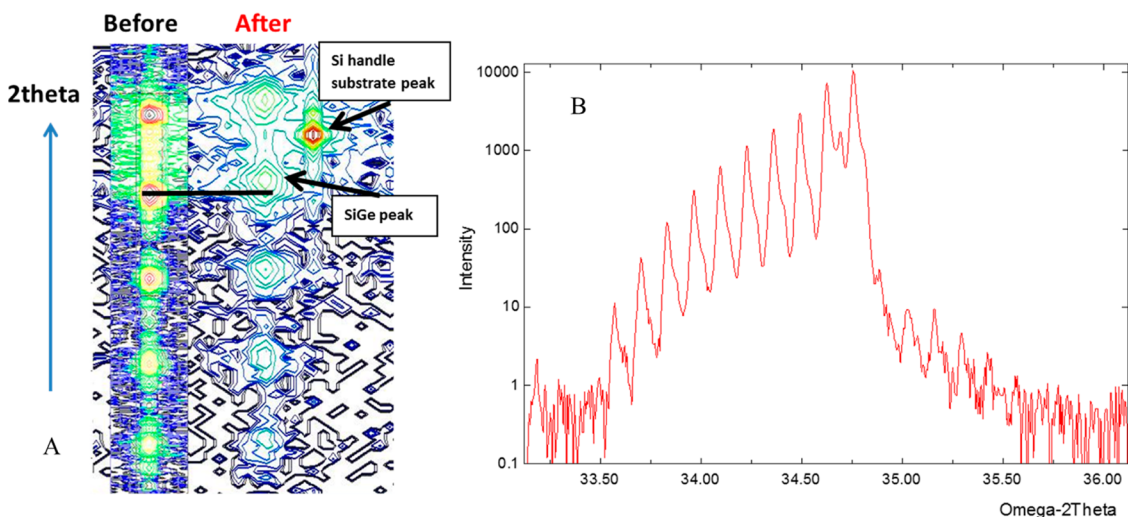


Figure 4. X-ray diffraction results from a QW NM sample at different stages of its fabrication process. (A) XRD reciprocal-space maps of the initial 5-period SiGe/Si QW structure measured before and after release from the SOI substrate via wet etching of the BOX layer. The Si handle substrate peak is also present in the “Before” scan but is cut off. (B) High-resolution omega/2theta XRD scan of the same sample after growth of 40 additional QW periods. The subsidiary maxima here are no longer resolvable because of the much larger number of periods.

of tensile strain in the Si template and barrier layers, until the in-plane lattice constant reaches a final value that produces zero net strain per period. This expected behavior is confirmed by the XRD reciprocal-space maps shown in Figure 4A: an upward shift of the SiGe peak is clearly observed in the map measured after NM release (relative to the map measured before release), which is consistent with compressive-strain relaxation in the SiGe layers.

After the BOX is fully dissolved in the wet etch, the 5-period NMs (with a total thickness of ~ 200 nm) settle on (and weakly bond to) the underlying Si substrate, where they are more firmly bonded by annealing at 450 °C for 1 h. The end result is a set of closely spaced rectangular-shaped membranes (with approximate lateral dimensions of 3×4 mm²) attached to the Si surface, as shown schematically in Figure 2D. It should be noted that in these NMs the SOI Si template layer is used as the first barrier, and the 5-period epitaxial film is terminated with a Si layer of the same thickness (17 nm). As a result of this symmetric configuration, no curling or folding of the NMs takes place during strain relaxation.²⁰ The Si substrate carrying the NMs is then transferred back into the LPCVD chamber where 40 additional QW periods are grown under the same conditions as the initial 5 periods (Figure 2E). Because of the aforementioned elastic relaxation, the 40 QWs grown on the NMs are fully strain compensated so that no net strain accumulates with increasing film thickness. As a result, no plastic deformation leading to misfit dislocations is expected to occur, despite the relatively large number of QWs. Figure 4B shows XRD data illustrating the structural quality of the resulting 45-period structure. Subsidiary maxima are no longer observable because they are too closely spaced (due to

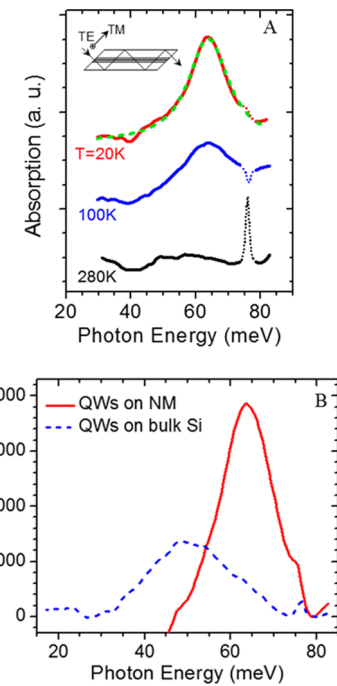


Figure 5. ISB absorption properties of the QW NM sample investigated in this work. (A) TM-polarized inverse transmission spectra measured at different heat-sink temperatures. Inset: experimental geometry used in these measurements. (B) Low-temperature (20 K) absorption coefficient of the same sample (solid line) and of a similar QW structure grown on a bulk Si substrate (dashed line).

the larger number of periods), but the sharpness and uniform spacing of the superlattice peaks again indicate high crystalline quality.

The far-infrared absorption properties of these multiple-QW structures were investigated using Fourier transform infrared (FTIR) spectroscopy, as described in

the Methods section. In Figure 5A we show the TM-polarized inverse transmission spectra of the sample of Figure 4 at different temperatures, normalized to those of a nominally identical sample without any QWs. A very pronounced absorption peak is clearly observed in the trace measured at 20 K, centered at a photon energy of about 64 meV, in relatively good agreement with the calculated HH1–HH2 ISB absorption energy of 58 meV. This feature is found to decrease rapidly with increasing temperature, as expected for ISB transitions at such long wavelengths, owing to thermal population of the excited subbands. Furthermore, no similar absorption peak was detected using TE-polarized incident light in the same experimental configuration, consistent with the previously discussed selection rules of HH ISB transitions. The much narrower feature near 76 meV observed in the traces of Figure 5A (plotted with a thin dotted line) is attributed to phonon absorption in the QWs under study and/or in the substrate,²¹ and therefore is not relevant to the present discussion.

The green dashed line in the same figure is a Lorentzian fit to the low-temperature spectrum, showing a remarkable agreement with the experimental data. The important conclusion is that ISB transitions in this sample are homogeneously broadened, which implies that in-plane and well-to-well thickness fluctuations (the dominant source of inhomogeneous broadening in multiple-QW samples)¹⁹ are negligible. This observation strongly substantiates the high structural quality of these strain compensated QWs grown on lattice-matched NMs. Furthermore, a relatively narrow ISB absorption line width of 15 meV fwhm is obtained from the Lorentzian fit. This value is smaller than what has been reported so far with similar SiGe/Si QWs grown on rigid Si substrates (over 20 meV in ref 18), despite the use in the latter work of fewer QW periods (10) grown by molecular beam epitaxy (MBE), which generally provides superior control of the QW growth parameters. Linewidths similar to the Lorentzian fit of Figure 5A have been reported with QWs deposited on graded SiGe buffer layers, but again grown by MBE and consisting of only 10 periods (separated by additional strain compensating buffer layers).²² Regarding the detailed origin of our measured line width, the most likely dominant contribution is scattering from interface roughness (which produces homogeneous broadening as long as its lateral length scale is smaller than the carrier wavelength).¹⁹

For a more direct comparison, we have also measured the ISB absorption properties of a similar multiple-QW structure grown with our LPCVD system on a bulk Si substrate. Specifically, this sample contains 40 repetitions of 7.7-nm-thick $\text{Si}_{0.80}\text{Ge}_{0.20}$ wells separated by 33.9-nm-thick Si barriers, where again the layer thicknesses and compositions were determined from XRD measurements. The doping density and spatial distribution are nominally the same as in the QW NM

sample of Figure 1. In Figure 5B we plot the low-temperature absorption coefficient α of both structures versus photon energy, obtained from the measured transmission spectra as described in the Methods section. The solid line refers to the QW NM sample investigated throughout this work, while the dashed line refers to the QW sample on the bulk Si substrate just described. These results are clearly consistent with the notion that the QW NM sample features superior structural quality, leading to stronger and spectrally narrower ISB absorption, compared to the QWs grown on the bulk Si substrate. In fact, the absorption line shape measured with the latter sample is markedly non-Lorentzian with a larger fwhm of 23 meV. This observation suggests large variations in layer thicknesses, as one would expect in a thick multiple-QW structure in the presence of strain relaxation *via* plastic deformation. As discussed throughout this work, the key motivation for growing QWs on a lattice-matched NM is to avoid such relaxation phenomena, and the experimental results of Figure 5B appear to support this expectation.

The absorption spectrum of the bulk-Si QW sample (peaked at 51 meV) is also found to be red-shifted compared to that of the QW NM (peaked at 64 meV), consistent with the larger measured QW thickness of the former structure (7.7 *versus* 7.0 nm) and the resulting decrease in ISB energy separations. Specifically, calculations based on the 6×6 Luttinger-Kohn model used in this work predict a value of 49 meV for the HH1–HH2 ISB absorption energy of the bulk-Si QW structure, in good agreement with the experimental results. In the case of the QW NM sample, the calculated absorption energy is 58 meV (as already discussed), which again is reasonably close to the measured value. In contrast, we note that the peak absorption coefficients of Figure 5B are substantially larger than theoretical predictions (as plotted in Figure 1D for the case of the QW NM structure). This discrepancy may be partly attributed to differences between the materials and structural parameters used in the simulations (including the details of the incident-light propagation in the sample) and their actual values. In addition, it has been shown that the combination of strong subband nonparabolicities and many-body interactions can result in substantially larger absorption values compared to predictions based on a single-particle picture.²³ These interactions may be important in the present context where we employ highly nonparabolic HH subbands (e.g., see Figure 1C) with relatively high carrier densities of about $1 \times 10^{12} \text{ cm}^{-2}$ per well. While inclusion of many-body effects (beyond the depolarization and exciton shifts of the absorption energy) requires computational tools that are beyond the scope of this work, it is possible that such effects may play a role in the observed discrepancy.

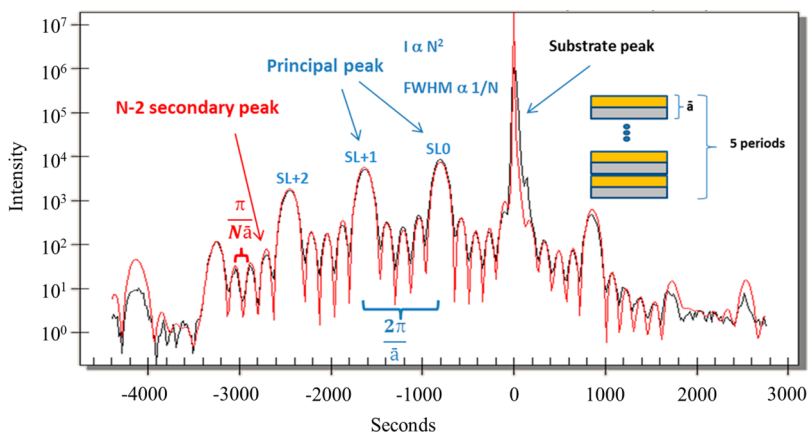


Figure 6. XRD scan from a 5-period SiGe/Si QW structure grown on a bulk Si substrate for calibration purposes. The experimental data are fit to determine the layer thicknesses, compositions, and average strain.

CONCLUSION

We have shown that the use of elastically strain relaxed NMs as the growth substrate produces a tangible improvement in the materials quality of highly lattice mismatched SiGe/Si QWs, specifically for far-infrared ISB device applications. These NMs consist of a few repetitions of the desired QW structure grown on the Si template layer of an SOI substrate, with overall thickness below the threshold for strain-induced plastic deformation. When the NM is released from the host wafer by etching the underlying BOX, elastic strain relaxation occurs *via* strain sharing among the constituent layers. The end result is therefore a dislocation-free NM that is perfectly lattice matched to the desired QW structure, so that an arbitrarily large number of additional QWs can in principle be grown over it without any strain accumulation. In the present work, this approach is used to develop a 45-period multiple-QW structure providing strong ISB absorption at a far-infrared wavelength near $20\text{ }\mu\text{m}$. The high structural quality of the resulting sample is confirmed *via* optical transmission spectroscopy measurements, which reveal a pronounced absorption peak with markedly Lorentzian line shape and substantially smaller spectral width compared to similar samples grown on bulk Si substrates. The same idea can be applied to more complex periodic QW structures, as long as the thickness of a single period is less than the plastic-deformation threshold. This approach is therefore promising for the development of Si-based QC lasers, which in turn would allow taking advantage of the nonpolar nature and intrinsic CMOS compatibility of the SiGe materials system for applications in THz photonics. Furthermore, the same approach can also be extended to a wide range of other materials systems, for any application where strain accumulation due to lattice mismatch with the epitaxial substrate is a limiting factor.

MATERIALS AND METHODS

Multiple-Quantum-Well Nanomembrane Fabrication. Fabrication of the strain compensated multiple-QW NMs

starts with a (001) SOI wafer having a $\sim 25\text{-nm}$ -thick Si template layer and a 150-nm -thick BOX layer (Figure 2A). The SOI wafer is diced into strips 8 mm wide and 42 mm long, which are then cleaned using the following standard procedure: (1) 20 s in 10% HF, (2) 10 min in Piranha clean, (3) 15 min in standard clean 1 (SC1), and (4) 20 s in 10% HF (with a 5-min DI water rinse between each step). Before growing the epitaxial films, the Si template layer is further thinned down to the desired thickness using plasma etching (Figure 2B). Next, a 5-period SiGe/Si QW structure is grown on the strip using LPCVD with SiH_4 , GeH_4 , and B_2H_6 as the precursor gases (Figure 2C). The growth temperature is about $620\text{ }^\circ\text{C}$ and the growth rate is 3 nm/min . It should be noted that in this initial SiGe/Si QW structure the (undoped) Si template layer of the SOI wafer is used as the first barrier. The as-grown film is then patterned by optical lithography to produce several rectangular-shaped membranes (with approximate lateral dimensions of $3 \times 4\text{ mm}^2$), each featuring a square-periodic array of small etchant-access holes through the epitaxial material (with spacing ranging from 50 to $200\text{ }\mu\text{m}$). Next, HF is used to completely etch away the BOX. As a result, the membranes are released in place and settle on the underlying Si substrate, where they are more firmly bonded by annealing at $450\text{ }^\circ\text{C}$ for 1 h (Figure 2D). Finally, the Si strip carrying the NMs is cleaned using the same standard procedure just described, and is transferred back into the LPCVD chamber for the subsequent growth of 40 additional QW periods with the same growth parameters (Figure 2E).

X-ray Diffraction Measurements. The structural properties of the SiGe/Si QWs are characterized with high-resolution XRD (Phillips Panalytical X'Pert PRO). Specifically, $\theta/2\theta$ line scans around the (004) reflection are measured and then fit to simulation results in order to extract the Ge composition of the SiGe wells and the layer thicknesses. This procedure was initially applied to several test samples consisting of a few SiGe/Si QW periods grown on bulk Si substrates, in order to

calibrate the growth parameters to obtain the desired thicknesses and compositions (see Figure 6). Reciprocal-space maps around the (004) reflection are also measured. They provide information about compressive-strain relaxation in the SiGe layers after NM release (Figure 4A).

Far-Infrared Absorption Spectroscopy. To measure the far-infrared absorption spectra of the QW NMs, the Si carrier wafer is diced along the boundaries of each NM, and the resulting samples are processed in a multipass wedge geometry with two opposite facets lapped at 45°. Next, two such samples are pressed against each other (with the QW NMs in between, as indicated schematically in the inset of Figure 5A), and then mounted on the coldfinger of a continuous-flow liquid-helium cryostat. This configuration allows displacing the QWs from the sample-air interfaces (where the electromagnetic boundary conditions require the TM component of the incident light to be nearly zero), without the need to grow unrealistically thick epitaxial cap layers.²⁴ As a result, it can substantially increase the overall TM light intensity in the QWs and therefore produce strong absorption from the TM-polarized HH ISB transitions under study. Furthermore, this experimental geometry effectively doubles the thickness of the absorbing layer (which becomes equivalent to 90 QW periods in the present case). The cryostat-mounted samples are finally placed in a beam condenser inside the sample compartment of an FTIR spectrometer, where light from a Globar source is coupled in and out at normal incidence through the 45°-facets and then detected with a liquid-helium-cooled Si bolometer. A wire-grid polarizer placed before the sample is used to discriminate between TE and TM polarizations. To subtract off background features, the resulting transmission spectra are normalized to similarly measured spectra obtained with a nominally identical sample without the QWs.

The absorption spectra $\alpha(\hbar\omega)$ plotted in Figure 5B were computed from the normalized transmission spectra $T(\hbar\omega)$ using the following relationship¹⁹

$$T = \exp(-\alpha MN_{\text{QW}}L_{\text{QW}}C/\sqrt{2})$$

In this equation, M is the number of times the incident light travels through the QWs in the multipass sample geometry of Figure 5A, which is approximately equal to the sample length divided by its thickness; N_{QW} is the number of QWs probed in each pass; L_{QW} is the thickness of the well layers as measured via XRD; the factor of $1/\sqrt{2}$ is a coupling constant that accounts for the direction and polarization of the incident light relative to the QW growth axis; and C is a dimensionless constant ≤ 2 that depends on the spatial overlap between the QWs and the standing-wave pattern produced in the sample by the incident light. As the latter parameter is not immediately known without

detailed electromagnetic simulations of the transmission measurements, here we assume a value of 2, which corresponds to optimal positioning of the QWs with respect to the optical-field profile.¹⁹ In any case, because the same experimental geometry was used to study both samples of Figure 5B, we expect this constant C to be the same for both traces. Therefore, its exact value does not affect the comparison between the two absorption spectra.

Conflict of Interest: The authors declare no competing financial interest.

Acknowledgment. This work was primarily supported by the National Science Foundation under Grant No. DMR-0907296. Development and maintenance of the growth facilities used in this work was supported by DOE, Grant No. DE-FG02-03ER46028. P.S. is supported by a Royal Thai Fellowship.

REFERENCES AND NOTES

1. Sigg, H. Intersubband Transitions in Si/SiGe Heterojunctions, Quantum Dots, and Quantum Wells. In *Intersubband Transitions in Semiconductor Quantum Structures*; Paiella, R., Ed.; McGraw-Hill: New York, 2006; pp 347–388.
2. Köhler, R.; Tredicucci, A.; Beltram, F.; Beere, H. E.; Linfield, E. H.; Davies, A. G.; Ritchie, D. A.; Iotti, R. C.; Rossi, F. Terahertz Semiconductor-Heterostructure Laser. *Nature* **2002**, *417*, 156–159.
3. Williams, B. S. Terahertz Quantum-Cascade Lasers. *Nat. Photonics* **2007**, *1*, 517–525.
4. Lee, M.; Wanke, M. C. Searching for a Solid-State Terahertz Technology. *Science* **2007**, *316*, 64–65.
5. Dehlinger, G.; Diehl, L.; Gennser, U.; Sigg, H.; Faist, J.; Ensslin, K.; Grützmacher, D.; Müller, E. Intersubband Electroluminescence from Silicon-Based Quantum Cascade Structures. *Science* **2000**, *290*, 2277–2280.
6. Bormann, I.; Brunner, K.; Hackenbuchner, S.; Zandler, G.; Abstreiter, G.; Schmutz, S.; Wegscheider, W. Midinfrared Intersubband Electroluminescence of Si/SiGe Quantum Cascade Structures. *Appl. Phys. Lett.* **2002**, *80*, 2260–2262.
7. Diehl, L.; Menteşe, S.; Müller, E.; Grützmacher, D.; Sigg, H.; Gennser, U.; Sagnes, I.; Campidelli, Y.; Kermarrec, O.; Bensahel, D.; et al. Electroluminescence from Strain-Compensated $\text{Si}_{0.2}\text{Ge}_{0.8}/\text{Si}$ Quantum-Cascade Structures Based on Bound-to-Continuum Transitions. *Appl. Phys. Lett.* **2002**, *81*, 4700–4702.
8. Lynch, S. A.; Bates, R.; Paul, D. J.; Norris, D. J.; Cullis, A. G.; Ikoníć, Z.; Kelsall, R. W.; Harrison, P.; Arnone, D. D.; Pidgeon, C. R. Intersubband Electroluminescence from Si/SiGe Cascade Emitters at Terahertz Frequencies. *Appl. Phys. Lett.* **2002**, *81*, 1543–1545.
9. Karunasiri, R. P. G.; Park, J. S.; Mii, Y. J.; Wang, K. L. Intersubband Absorption in $\text{Si}_{1-x}\text{Ge}_x/\text{Si}$ Multiple Quantum Wells. *Appl. Phys. Lett.* **1990**, *57*, 2585–2587.
10. Friedman, L.; Soref, R. A.; Sun, G. Silicon-Based Intermini-band Infrared Laser. *J. Appl. Phys.* **1998**, *83*, 3480–3485.
11. Driscoll, K.; Paiella, R. Silicon-Based Injection Lasers Using Electronic Intersubband Transitions in the L Valleys. *Appl. Phys. Lett.* **2006**, *89*, 191110–191110–3.
12. Valavanis, A.; Dinh, T. V.; Lever, L. J. M.; Ikoníć, Z.; Kelsall, R. W. Material Configurations for N-Type Silicon-Based Terahertz Quantum Cascade Lasers. *Phys. Rev. B* **2011**, *83*, 195321–195321–8.
13. Ortolani, M.; Stehr, D.; Wagner, M.; Helm, M.; Pizzi, G.; Virgilio, M.; Grosso, G.; Capellini, G.; De Seta, M. Long Intersubband Relaxation Times in N-Type Germanium Quantum Wells. *Appl. Phys. Lett.* **2011**, *99*, 201101–201101–3.
14. Gallas, B.; Hartmann, J. M.; Berbezíer, I.; Abdallah, M.; Zhang, J.; Harris, J. J.; Joyce, B. A. Influence of Misfit and Threading Dislocations on the Surface Morphology of SiGe Graded-Layers. *J. Cryst. Growth* **1999**, *201*, 547–550.

15. Roberts, M. M.; Klein, L. J.; Savage, D. E.; Slinker, K. A.; Friesen, M.; Celler, G.; Eriksson, M. A.; Lagally, M. G. Elastically Relaxed Free-Standing Strained-Silicon Nanomembranes. *Nat. Mater.* **2006**, *5*, 388–393.
16. Rogers, J. A.; Lagally, M. G.; Nuzzo, R. G. Synthesis, Assembly, and Applications of Semiconductor Nanomembranes. *Nature* **2011**, *477*, 45–53.
17. Paskiewicz, D. M.; Tanto, B.; Savage, D. E.; Lagally, M. G. Defect-Free Single-Crystal SiGe: A New Material from Nanomembrane Strain Engineering. *ACS Nano* **2011**, *5*, 5814–5822.
18. Fromherz, T.; Koppensteiner, E.; Helm, M.; Bauer, G.; Nützel, J. F.; Abstreiter, G. Hole Energy Levels and Intersubband Absorption in Modulation-Doped Si/Si_{1-x}Ge_x Multiple Quantum Wells. *Phys. Rev. B* **1994**, *50*, 15073–15085.
19. Helm, M. The Basic Physics of Intersubband Transitions. In *Intersubband Transitions in Quantum Wells: Physics and Device Applications I*; Liu, H. C., Capasso, F., Eds.; Academic Press: San Diego, 2000; pp 1–100.
20. Huang, M.; Cavallo, F.; Liu, F.; Lagally, M. G. Nanomechanical Architecture of Semiconductor Nanomembranes. *Nanoscale* **2011**, *3*, 96–120.
21. University of Reading, Infrared Multilayer Laboratory. www.reading.ac.uk/infrared/library/infraredmaterials/ir-infraredmaterials-si.aspx.
22. Fromherz, T.; Meduña, M.; Bauer, G.; Borak, A.; Falub, C. V.; Tsujino, S.; Sigg, H.; Grützmacher, D. Intersubband Absorption of Strain-Compensated Si_{1-x}Ge_x Valence-Band Quantum Wells with 0.7 < x < 0.85. *J. Appl. Phys.* **2005**, *98*, 044501–044501–7.
23. Warburton, R. J.; Gauer, C.; Wixforth, A.; Kotthaus, J. P.; Brar, B.; Kroemer, H. Intersubband Resonances in InAs/AlSb Quantum Wells: Selection Rules, Matrix Elements, and the Depolarization Field. *Phys. Rev. B* **1996**, *53*, 7903–7910.
24. Machhadani, H.; Kotsar, Y.; Sakr, S.; Tchernycheva, M.; Colombelli, R.; Mangeney, J.; Bellet-Amalric, E.; Sarigiannidou, E.; Monroy, E.; Julien, F. H. Terahertz Intersubband Absorption in GaN/AlGaN Step Quantum Wells. *Appl. Phys. Lett.* **2010**, *97*, 191101–191101–3.